Bulletin of the Seismological Society of America, Vol. 75, No. 6, pp. 1765–1782, December 1985

FINITE-DIFFERENCE SEISMOGRAMS FOR *SH* WAVES

By John Vidale, Donald V. Helmberger, and Robert W. Clayton

Abstract

The accuracy of the finite-difference method for generating synthetic seismograms of *SH* wave propagation in cylindrically symmetric media is discussed. The finite-difference method has the advantage that arbitrary density and velocity fields in the medium may be specified. A point source is generated by a simple transformation of a line source. The accuracy of the finite-difference seismograms in flat- and dipping-layered media is confirmed by comparison with the generalized ray method. A source radiation pattern is inserted by introducing a "near-field" which has permanent displacement near the source.

Strong motion synthetics are constructed with this new method for the 1968 Borrego Mountain earthquake as recorded at El Centro. Good fits to the data are achieved using the laterally varying model determined by a detailed refraction survey and the source parameters determined by teleseismic waveform modeling. Shallow faulting is no longer necessary to explain the long-period surface-wave development.

Introduction

The understanding of earthquake-generated motions has improved significantly in recent years. This progress is due in large part to the refinement of methods for generating synthetic seismograms to compare with an ever-growing collection of observations. Synthetic seismograms are generally used in iterative forward modeling schemes where the source and medium parameters are perturbed until a best match with the data is obtained. This technique has proven to be powerful for determining subtle features of both the source and the medium. The technique is limited, however, by the range of earth structure that can be modeled. Traditionally, the medium models have been a stack of homogeneous layers, which is inadequate for laterally heterogeneous structures such as ocean-continent transition zones and basin structures.

In this paper, we relax some of these limitations by allowing dipping structure and introducing a procedure whereby two-dimensional finite-difference (FD) calculations can be mapped into synthetic seismograms with the proper point source shear dislocation characteristics. This procedure has the advantage of allowing for arbitrary density and velocity fields in two dimensions. In this paper, only *SH* waves (horizontally polarized shear waves) are treated but the method may be extended to *P-SV* waves.

In the first section, a procedure for mapping line source responses (the source used by the FD method) to point source responses with a radiation pattern is given. The similarity of the generalized ray theory (GRT) expressions for strike-slip and dip-slip types of sources leads to the identification of the vertical radiation patterns required for the line-source FD source. In the next section, FD seismograms generated using these radiation patterns are seen to agree well with GRT seismograms. In the last section, this technique is applied to model the seismogram recorded at El Centro for the 1968 Borrego mountain event.

Source Representation

The source representation described in this section is the first, to our knowledge, that allows the use of two-dimensional FD or finite-element programs to create

point source synthetic seismograms that may be compared with data for both amplitude and waveform. This source is derived by matching previously known first-term asymptotic solutions (e.g., Helmberger, 1983) with the "pseudo-near-field" terms necessary to produce radiation patterns with two-dimensional codes.

The *SH* displacement in a horizontally layered medium from a buried point dislocation source can be conveniently expressed as a sum of generalized rays (Helmberger and Malone, 1975)

$$v(t) = \frac{M_0}{4\pi\rho_0}\frac{d}{dt}\left[\frac{d\,D(t)}{dt} * \sum_{j=1}^{2} A_{j+3}(\theta, \lambda, \delta)V_j(t)\right] \tag{1}$$

where

$$V_j(t) = \sqrt{\frac{2}{r}}\frac{1}{\pi}\left[\frac{2}{\sqrt{t}} * \sum_{i=1}^{n}\left(\frac{p^{3/2}}{\eta_2} SH_j(p)\ \text{II}\ \frac{dp}{dt}\right)_i\right] \tag{2}$$

are the generalized rays, t is time, r is horizontal distance between source and receiver, n is the number of rays used to approximate the response, M_0 is seismic moment, ρ_0 is density at the source, $D(t)$ is the dislocation history across the fault

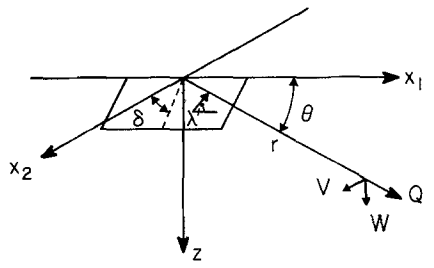

FIG. 1. Description of conventions for mechanism and orientation.

element, and $\frac{d\,D(t)}{dt}$ is the far-field time function. The area under $\frac{d\,D(t)}{dt}$ is normalized to one. The dependence on azimuth and mechanism are contained in the terms

$$A_4 = \cos 2\theta \cos\lambda \sin\delta - \tfrac{1}{2}\sin 2\theta \sin\lambda \sin 2\delta \tag{3a}$$

$$A_5 = \sin\theta \cos\lambda \cos\delta - \cos\theta \sin\lambda \cos 2\delta \tag{3b}$$

where θ is the strike from the end of the fault, λ is the rake angle, and δ is the dip angle. Figure 1 shows the fault orientation conventions. The strike-slip and dip-slip vertical radiation patterns are, respectively,

$$SH_1 = \frac{1}{\beta_0^2} \tag{4a}$$

and

$$SH_2 = \frac{-\epsilon\eta}{\beta_0^2 p} \tag{4b}$$

where β_0 is the shear wave velocity at the source. For receivers above the source, ϵ is -1 and is $+1$ for receivers below the source. Π_i is the product of transmission and reflection coefficients for the ith ray. In a whole-space, there is only one ray, however, and

$$p = \frac{\sin \alpha}{\beta}$$

is the ray parameter, and

$$\eta = \frac{\cos \alpha}{\beta}$$

$$t = pr + \eta h$$

where α is the angle between the vertical and a line connecting the source and receiver that is shown in Figure 2, and $\frac{dp}{dt}$ is determined from $t(p)$.

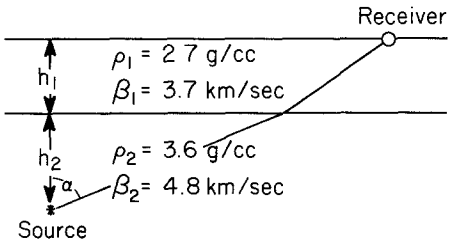

FIG. 2. Flat-layer over a half-space geometry with shear wave velocities and densities. The crust has h_1 of 9 km with a density ρ_1 of 2.7 gm/cm^3 and a shear wave velocity β_1 of 3.7 km/sec, and the underlying upper mantle has ρ_2 of 3.6 gm/cm^3 and β_2 of 4.8 km/sec. The source is placed 18 km below the surface, or h_2 is 9 km.

Note that $V_1(t)$ and $V_2(t)$ do not depend on azimuth or mechanism but contain only the vertical radiation patterns. This separation allows the two V_j's to be constructed by equation (2), and the azimuthal pattern and mechanism to be calculated by equation (1).

For $t_r \gg T$, where T is the source duration and t_r is $\frac{R}{\beta}$, equation (2) simplifies to

$$V_1 = \frac{\sin \alpha}{\beta^3} \frac{H(t - t_r)}{R} \tag{5}$$

for a strike-slip fault and

$$V_2 = \frac{\cos \alpha}{\beta^3} \frac{H(t - t_r)}{R} \tag{6}$$

for a dip-slip fault where R is the source to receiver distance. Thus, the trigonometric functions specify the well-known radiation patterns. Substituting (5) into (1) and letting $\lambda = 0°$ and $\delta = 90°$ for the strike-slip case, the displacement in centimeters

is

$$v(r, z, t) = \frac{M_0}{4\pi\rho_0} F_0 \left(\frac{\sin \alpha}{\beta^3}\right) \cos 2\theta \frac{d\, D(t - t_r)}{dt} \frac{1}{\gamma R} \tag{7}$$

where β is given in kilometers/second, R in kilometers, and $F_0 = 10^{-20}$ for unit conversion and $\gamma = D(\infty)$ for strength normalization.

To maintain the correct behavior for large R, we need to include a pseudo-near-field term (Helmberger, 1983)

$$V_1 = \frac{1}{\beta^2 R} \mathrm{Re}(p)\mathrm{Im}\left(\frac{1}{\eta} \frac{dp}{dt}\right) \tag{8a}$$

that simplifies to

$$V_1 = \frac{t}{\beta^2} \frac{\sin \alpha}{R} \frac{H(t - t_r)}{R} \tag{8b}$$

and

$$V_2 = \frac{1}{\beta^2 R} \mathrm{Re}(\eta)\mathrm{Im}\left(\frac{1}{\eta} \frac{dp}{dt}\right) \tag{9a}$$

that simplifies to

$$V_2 = \frac{t}{\beta^2} \frac{\cos \alpha}{R} \frac{H(t - t_r)}{R}. \tag{9b}$$

These are not the complete near-field effects but only compatible with the asymptotic nature of the solution. If we were to include the exact near-field solution for the radiated SH waves, we would have to include the near-field contributions of P and SV as well (Helmberger and Harkrider, 1978).

The solution for a symmetric line source assuming a horizontally layered media becomes

$$\Phi(r, z, t) = \frac{d}{dt} [f(t) * \Psi] \tag{10}$$

$$\Psi = 2 \sum_{i=1}^{n} \left(\frac{\Pi}{\eta_2} \frac{dp}{dt}\right)_i \tag{11}$$

with the same definitions given for expressions (1) and (2).

A symmetric point or line source is easily grasped intuitively if the state variable is pressure in an acoustic problem, but a symmetric SH source is more difficult. A symmetric SH line source may be visualized as being caused by a tug on the line source. A symmetric SH point source, however, must simply be considered to have the same SH amplitude and sign for every take-off angle and azimuth.

For a whole-space

$$\Psi = \frac{H\left(t - \frac{R}{\beta}\right)}{\sqrt{t^2 - \frac{R^2}{\beta^2}}}. \tag{12}$$

Substituting (12) into (10), we obtain

$$\Phi(r, z, t) = \frac{f\left(t - \frac{R}{\beta}\right)}{\sqrt{t^2 - \frac{R^2}{\beta^2}}} \tag{13}$$

that is the well-known line source solution. By comparing expression (11) with (2) and the near-field effects just discussed, we can determine the constants and mapping required, namely let

$$V_j(t) = \frac{1}{\sqrt{t}} * \Phi_j \tag{14}$$

where Φ_j is the output of the FD code with the following source descriptions

$$\Phi_1 = \Phi_0 \left(\frac{\sin \alpha}{R}\right) t \frac{H(t - t_r)}{\sqrt{t^2 - \frac{R^2}{\beta^2}}} \tag{15a}$$

for the strike-slip orientation and

$$\Phi_2 = \Phi_0 \left(\frac{\cos \alpha}{R}\right) t \frac{H(t - t_r)}{\sqrt{t^2 - \frac{R^2}{\beta^2}}} \tag{15b}$$

for the dip-slip. The constant is

$$\Phi_0 = \beta^{-5/2} \sqrt{\frac{2}{R}}. \tag{16}$$

In other words, Φ_1 and Φ_2 specify the displacement that is imposed in the source region, which must have constant velocity and density equations (15a) and (15b) represent a whole-space solution. The FD code propagates the energy through the laterally heterogeneous structure to the receivers. The point source seismograms from shear dislocations are generated with equation (1) using the V_j from equation (14) which use Φ_j from the FD code.

The separation of variables between the V_j's and the A_j's allows two different ways to use equation (1). If synthetic seismograms for several different mechanisms are desired, one calculates both V_j's from two FD runs and combines them with the appropriate A_4 and A_5 for each seismogram. If only one seismogram is desired, one can combine the V_j's with the appropriate A's to create the source and only run the FD code once.

We will next discuss the FD method and then compare FD and line source GRT results.

FD Techniques

The FD *SH* code used is similar to the acoustic code described by Brown and Clayton (1977). The code is fourth order in accuracy of spatial derivatives (see Alford *et al.*, 1974, for definition and examples of order for FD codes). The fourth-order scheme reduces grid dispersion, which artificially slows down the propagation of the higher frequency waves. Figure 3 shows the relative error of the second- and fourth-order approximations. The fourth-order scheme allows propagation with

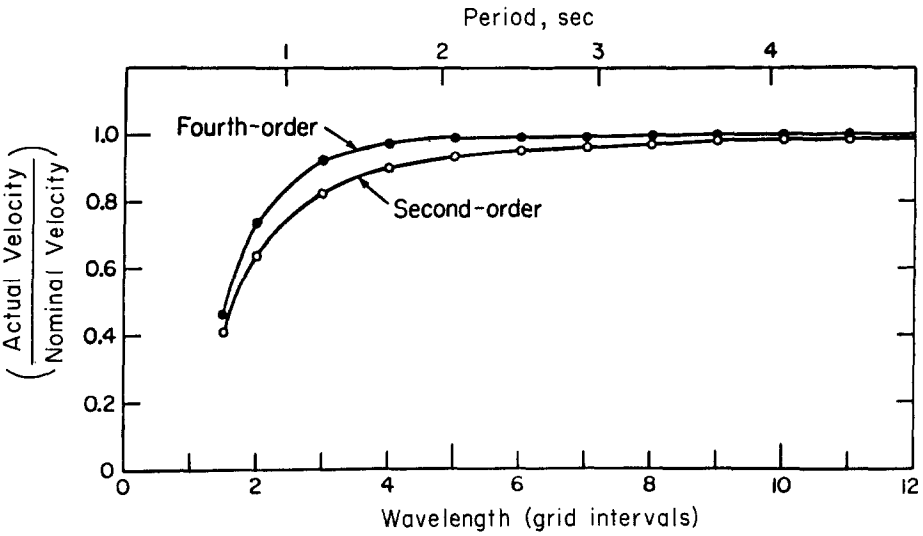

FIG. 3. Estimated spatial derivative divided by true spatial derivative plotted against wavelength measured in grid spaces on the *bottom* and period in seconds on the *top*. The line with solid circles shows the curve for second-order algorithms.

negligible dispersion for energy with wavelengths down to five grid points, or one-half the limit of 10 points per wavelength of a second-order scheme.

Absorbing boundary conditions are imposed on the sides and the bottom of the FD grid as described by Clayton and Engquist (1980), and the top of the grid is made a free surface for *SH* waves (reflection coefficient is equal to 1) by the method of Alterman and Karal (1968).

Several schemes for source insertion have been described in the literature. Imposing the displacement as a function of time either at one side or at the bottom of the box works if the source is too far from the receiver to be embedded in the box (see Boore, 1972, for example). A simpler approach imposes an initial displacement in a source region for the first two time steps and leaves the grid source-free for the remaining time steps (Alford *et al.*, 1974). A third method commonly used is described in Alterman and Karal (1968). In essence, it solves the wave propagation twice in the source region, once imposing the source and once without a source, and

combines the results so that the source region does not act as a rigid reflector. This method has the advantage that an arbitrary time function can be specified. We use the method of Alterman and Karal (1968), except that fourth- instead of second-order boundary conditions are used to match the source region with the surrounding region.

Figure 4 illustrates the explosive, strike-slip, and dip-slip sources that correspond to the sources described in equations (13), (15a), and (15b). all three sources have a transient wave that moves outward, but the sin θ (strike-slip) and cos θ (dip-slip) sources also have a two-lobed displacement pattern that is permanent. This permanent displacement is analogous to permanent deformation caused by movement

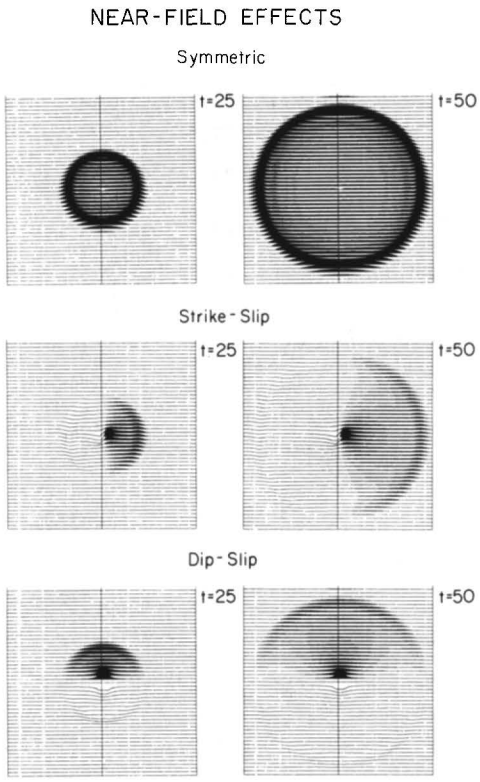

FIG. 4. Snapshots of displacements for the symmetric source, the sin θ mechanism source, and the cos θ mechanism source. The *left frames* show displacements after 25 timesteps, the *right* after 50. The amplitude scale is different for each plot. Positive displacements are filled in with black, but negative displacements are difficult to discern.

on a fault. The permanent displacement falls off with distance as r^{-1}, while the transient displacement falls off as $r^{-1/2}$.

The source for Figures 5 and 6 is symmetric and generated analytically by convolving an excitation function with the impulse response for a line source that is given in equation (13). Figures 7 through 10 use the dislocation sources given in equation (15).

Line source seismograms are described above, but point source seismograms are desired. Line source seismograms may be transformed to point source seismograms by equation (14) as described above. A linear sum of the two sets of point source seismograms can then be used to make seismograms for any strike, dip, and rake earthquake mechanism for a given velocity and density structure as given by equation (1).

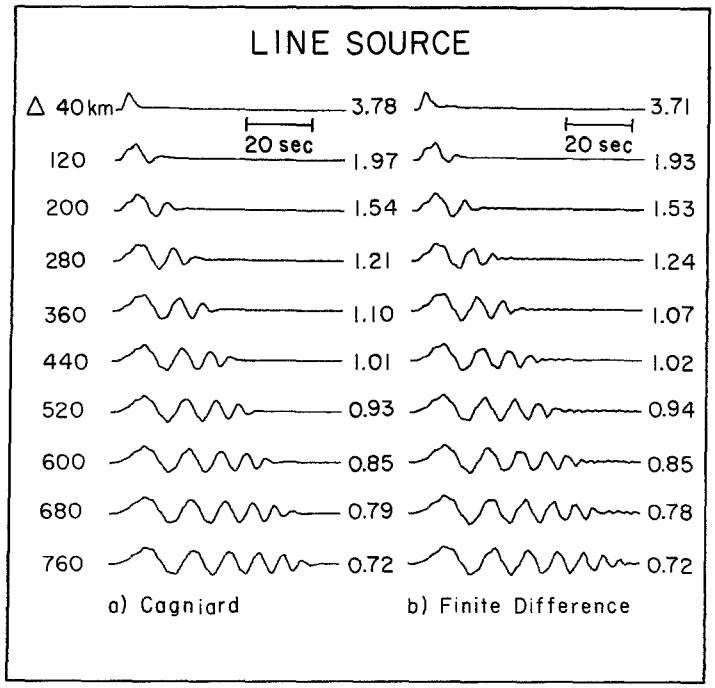

FIG. 5. Comparison of the line source synthetic seismograms generated by the GRT and FD methods. Results are for a 9-km-thick layer over a half-space. The source is 9 km below the layer, and the receivers are on the surface and range from 40 to 760 km in horizontal distance from the source. Both sets of seismograms are convolved with a trapezoidal time function. The amplitudes are absolute.

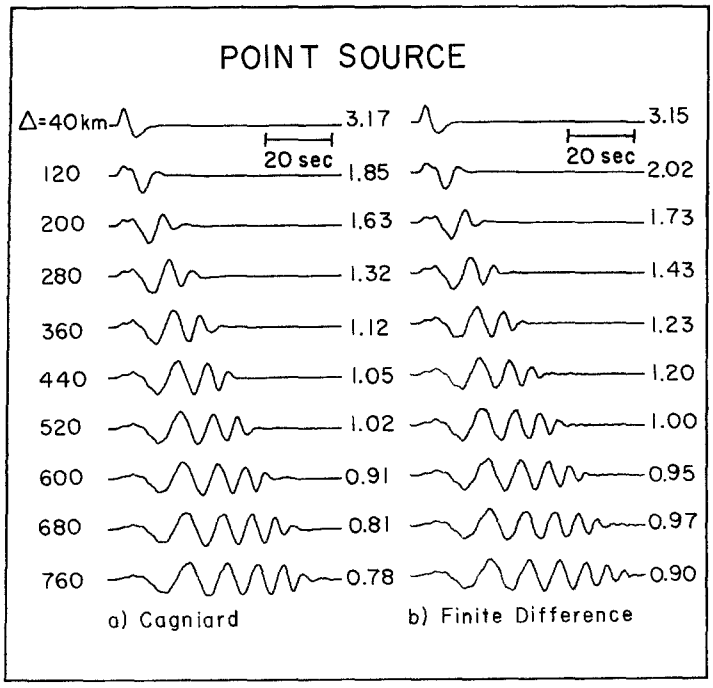

FIG. 6. Comparison of the point source synthetic seismograms generated by the GRT and FD methods for the same flat-layer geometry as is used for Figure 5. Amplitudes are absolute and may be scaled to moment.

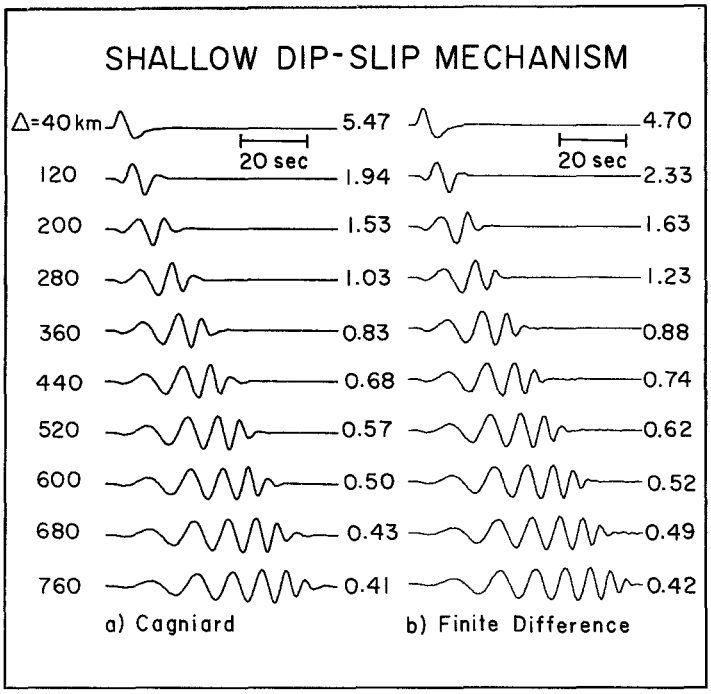

FIG. 7. Comparison of the point source cos θ mechanism synthetic seismograms generated by the GRT and FD methods for the same flat-layer geometry as is used for Figure 5.

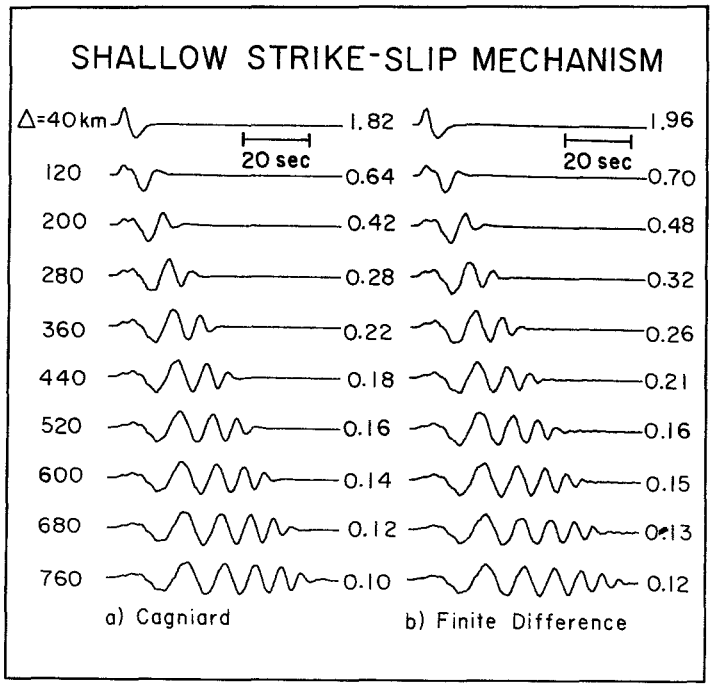

FIG. 8. Comparison of the point source sin θ mechanism synthetic seismograms generated by the GRT and FD methods for the same flat-layer geometry as is used for Figure 5.

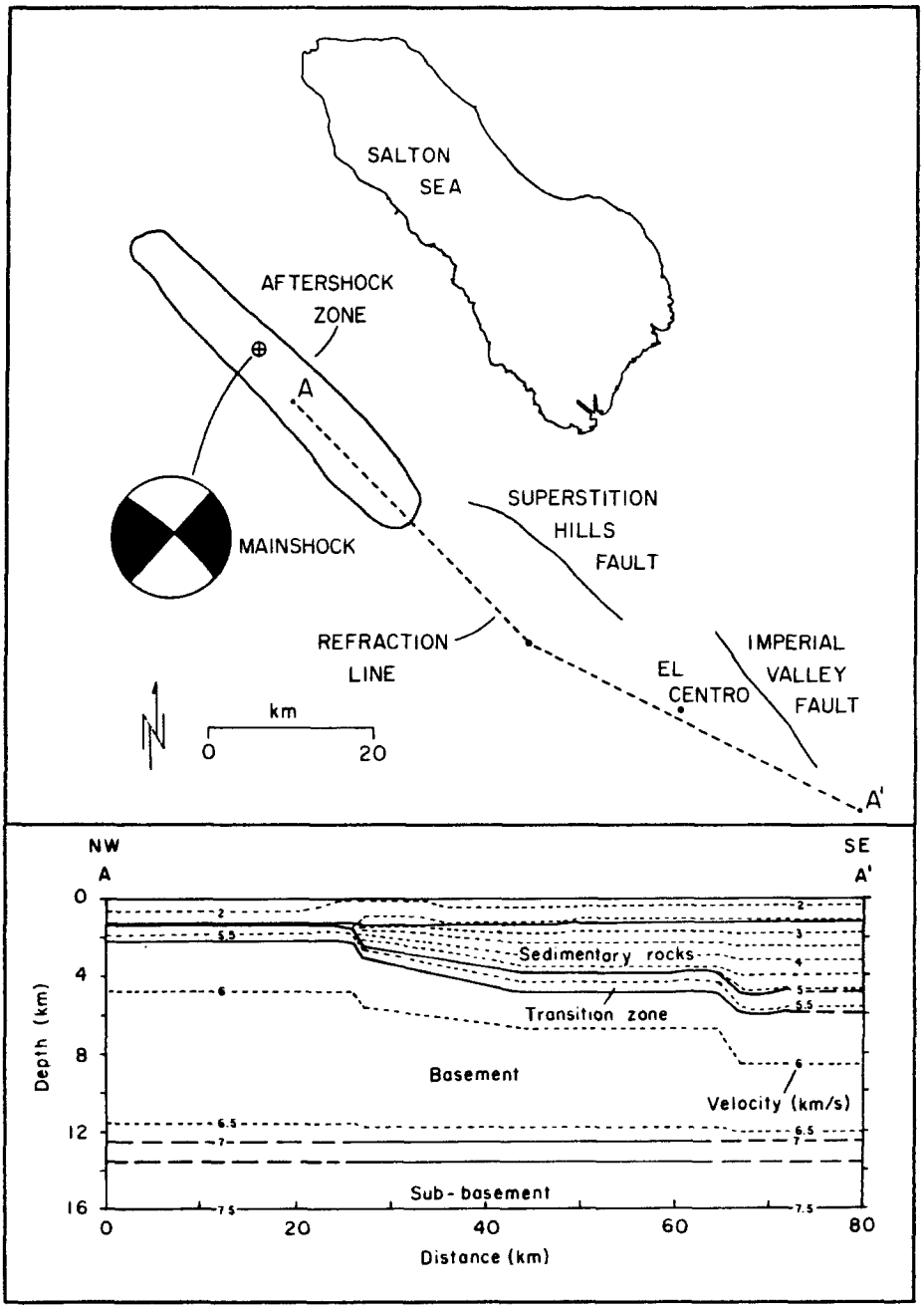

FIG. 9. Sketch map of the area of the Borrego Mountain main shock and the El Centro strong motion station. The aftershock zone and some of the faults in the area are shown. The cross-section shows the *P*-wave velocities estimated by Fuis *et al.* (1983) from refraction work along profile *A-A'*.

We use a trapezoid of 3-sec duration with 1-sec rise time and 1-sec fall time as an excitation function for the flat-layer models. The trapezoidal time functions filter out frequencies that would disperse in the grid and may be thought of as source time functions, as is common in modeling earthquake records (Langston and Helmberger, 1975).

Discussion

The FD code is compared with the flat-layer GRT code that has been well-tested (c.f. Apsel and Luco, 1983) for a model with one layer over a half-space that represents simple oceanic lithosphere. The geometry and media parameters are shown in Figure 2.

Receivers for the plots in Figures 5 through 10 are positioned on the surface at lateral distances of 40 to 760 km from the source. These plots are reduced by a 4.8 km/sec velocity.

Figure 5 contains synthetic seismograms for the line source problem with symmetric source. The results from the GRT code (Figure 5a) and the results from the FD code (Figure 5b) are in excellent agreement.

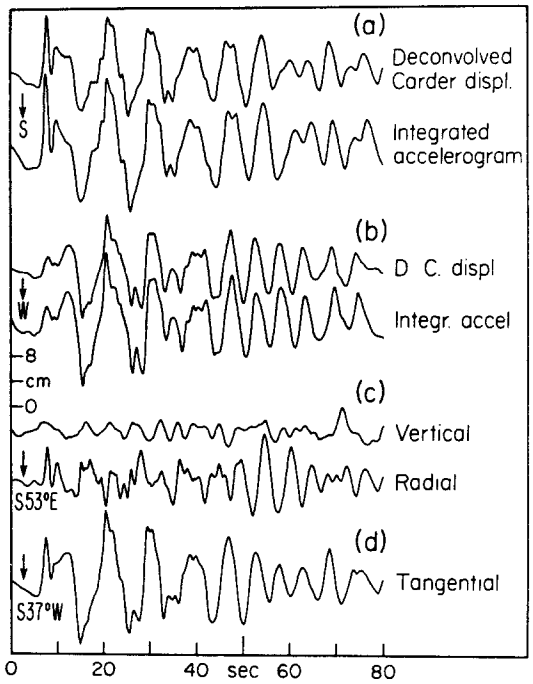

FIG. 10. Summary of observed ground motion. (a) Comparison of deconvolved Carder displacement meter record and integrated accelerogram for N-S component. (b) Comparison of deconvolved Carder displacement meter record and integrated accelerogram for E-W component. (c) Ground motion rotated into vertical, radial, and tangential components [from Heaton and Helmberger (1977)].

Amplitudes differ between the two sets of synthetics by no more than 3 per cent, and the detailed waveforms are nearly identical. Even the highest frequencies shown agree well for the first portion of each seismogram. The later portion of the seismograms shows some contamination by dispersed high-frequency energy. This agreement is consistent with Figure 3, which shows that the energy with periods above 2 sec should be propagated correctly. The discrepancies between the traces are high frequency and small.

The point source synthetics fare nearly as well. They are generated by equation (14), described above. The synthetics are convolved with the long-period WWSSN instrument response. The shortest and longest period energy is attenuated in transforming the line source seismograms to the point source seismograms and including the instrument response. The traces generated by the point-source, flat-

layer GRT program (Figure 6a) and those obtained by the transformation of the FD seismograms (Figure 6b) are in close agreement. The waveform agreement is excellent. The amplitudes agree to within 20 per cent in all cases.

The next question is whether the FD seismograms with sine and cosine vertical radiation patterns agree with their GRT equivalents. For Figures 7 and 8, the same flat-layer geometry described above is used. Figure 7 shows traces for the cos θ radiation pattern, and Figure 8 shows traces for the sin θ radiation pattern. The agreement in waveform is good, and again the amplitudes agree to within 20 per cent for all but the nearest offsets.

Some disagreement is expected for near-vertical takeoff angles because of a slight difference in geometrical spreading between the two-dimensional and three-dimensional geometries. For three-dimensional spreading, there should an additional factor of $\sqrt{\sin \alpha}$ in the vertical radiation pattern. This factor can be seen, for example, as an additional $\sqrt{p}$ for the point source that is not in the line source on p. 181 of Helmberger (1983). We are not able to simulate the additional factor of $\sqrt{\sin \alpha}$ because the expression is singular at α of 0° and 180° that introduces numerical problems. However, we are generally not interested in vertical paths since they are easily handled by other methods, see Scott and Helmberger (1983), for example.

Application to the Borrego Mountain Earthquake

We have developed above a method for constructing seismograms for general structures, but it remains to show that this flexibility aids in the interpretation of data. To show its usefulness, we will investigate the well-studied Borrego Mountain strong-motion recording from El Centro. Figure 9 shows the relative locations of the epicenter, major structures, and the receiver. The displacement data is summarized in Figure 10, which is taken from Heaton and Helmberger (1977). The agreement between the deconvolved Carder displacement record and the integrated accelerogram is excellent. El Centro is located along the strike of the fault, roughly 8° off, which places it near the *SH* maximum and a *P-SV* node. If the station were at a *P*-wave node on a flat-layered earth, one would expect the N-S and E-W traces to have the same waveform, and all the energy would rotate to the transverse component. For simplicity, we follow Ebel and Helmberger (1982) in modeling the first 50 sec of the N-S integrated accelerogram after dividing by cos 37°, which is the angle between the back-azimuth and north. This record is shown as the second trace of (a) in Figure 10 and again as trace (D) in Figure 12. For later times, the motion appears to arrive at the station mostly on the radial and would not be explainable with a two-dimensional *SH* model. The objective of this section is to investigate the effect of using the most recent data about the cross-sectional structure on the long-period motions, given the simple teleseismic source description.

One of the first teleseismic waveform modeling studies was conducted on this earthquake by Burdick and Mellman (1976). They modeled the long-perid *P* waveform with *P*, *pP*, and *sP* rays as well as the long-period *SH* waveform with *S* and *sS* rays. Their results suggest a zone of faulting around a depth of 8 km, with three distinct sources. Their first source has 75 per cent of the moment and has the expected focal mechanism. The other two subevents have unexpected mechanisms that may be a result of crustal phases produced by nonplanar structure and are less accepted by the seismological community. More recently, Ebel and Helmberger (1981) studied the *P*-wave complexity and found evidence for two asperities. Forward

and inverse modeling of the data suggest a two source model, each of less than 2-sec duration. The second source occurred about 2.2 sec after the first, and both events appear to be at a depth of 8 km. This complex source was used to synthesize the direct *SH* arrival on velocity and acceleration records with some success. The long-period teleseismic synthetics generated with the more complicated source model appears to agree well with the initial source found by Burdick and Mellman (1976).

Little evidence for shallow faulting is suggested by the teleseismic data. On the other hand, Heaton and Helmberger (1977) suggest substantial shallow faulting to explain the strength of the Love waves at El Centro. From a modeling point of view, one would expect the ratio of body waves to surface waves to be an excellent depth discriminant. However, a flat-layered model may not provide the appropriate Green's function in this particular path as suggested by the recent study of Fuis *et al.* (1983). We will investigate the properties of the more complicated Green's functions in this study using the first long-period source found by Burdick and Mellman (1976), namely a 0.1-, 1.0-, 4.0-sec trapezoid.

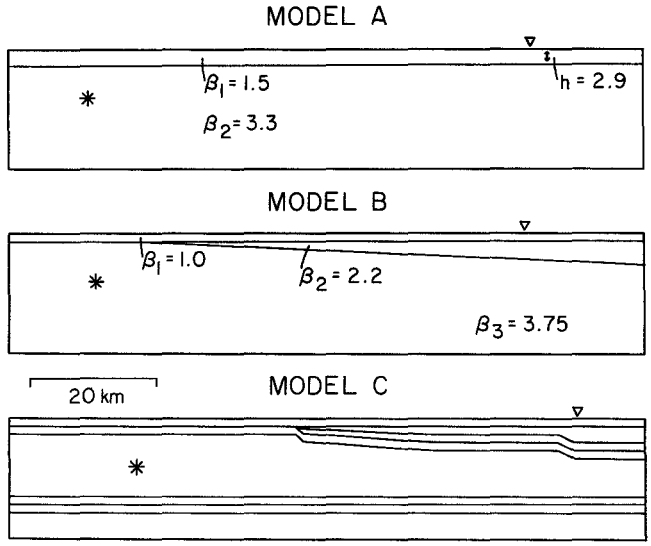

FIG. 11. Three models of the structure between the Borrego Mountain earthquake, shown by an asterisk, and the El Centro station, shown by a small triangle. There is no vertical exaggeration. The velocities and assumed densities for the profiles on the *left* and *right sides* of the model are given in Table 1.

Three structures are shown in Figure 11 that increase in verisimilitude as well as complexity from models A to C. Model A is the layer over a half-space used by Heaton and Helmberger (1977) and Swanger and Boore (1978). Model B is a more accurate dipping layer model. Model C is the *S*-wave version of the structure from Fuis *et al.* (1983). The *S*-wave velocities for profiles on the left and right sides of model C are given in Table 1. The ratio of *P*- to *S*-wave velocity is assumed to be $\sqrt{3}$ except in the top layer where it is taken to be 2.

A strike-slip source is introduced with the depth (8 km) and the time function (a 0.1-, 1.0-, 4.0-sec trapezoid) estimated from teleseismic studies (Burdick and Mellman, 1976). The resulting displacements for models A, B, and C are shown in Figure 12, A to C. The El Centro displacement record is shown in Figure 12D. The seismogram in Figure 12E results from a perturbation to model C discussed below.

The flat-layered model A generates the correct initial long-period displacement, as it was designed to do. There is little short-period energy, and the signal dies away too fast. The dipping-layer model B is seen to trap short-period energy in Figure 12B, as discussed below, but the long-period energy does not mimic that in the data.

The seismogram in Figure 12C from model C matches the first 20 sec of the data

TABLE 1

VELOCITIES IN MODEL C

S-Wave Velocity (km/sec)	Density (gm/cm^3)	Depth to Top of Layer (km)	
		Left Side	Right Side
1.0	1.4	0.	0.
1.55	1.9	1.6	1.6
1.8	2.0	—	3.8
3.0	2.3	1.8	5.0
3.75	2.7	2.6	6.2
4.0	2.8	12.2	12.2
4.125	2.8	12.6	12.6
4.25	2.9	13.2	13.2
4.375	2.95	13.8	13.8
4.5	3.0	14.2	14.2
4.625	3.1	14.6	14.6
4.75	3.2	15.2	15.2

Vidale *et al.*, 1985, in preparation.

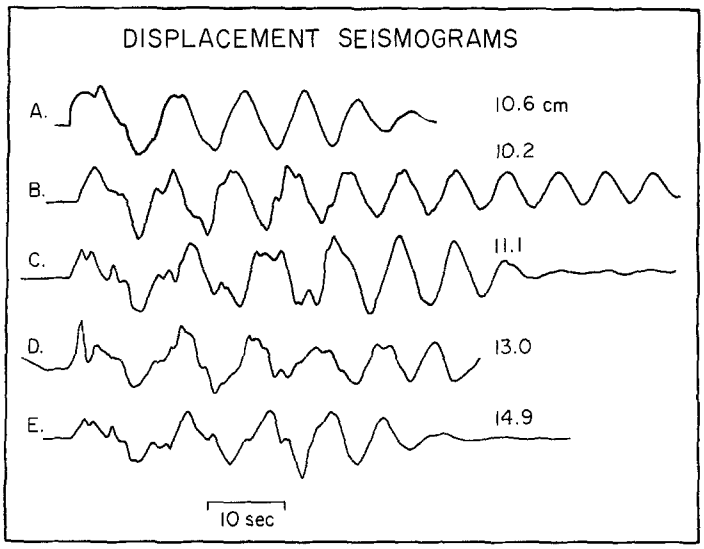

FIG. 12. The displacements at El Centro resulting from: (A) model A in Figure 11; (B) model B in Figure 11; (C) model C in Figure 11; (D) the actual earthquake; and (E) model C, but with the velocity of the top layer set to 1.2 km/sec instead of 1.0 km/sec. See text for detailed description.

reasonably well, aside from the initial pulse. The initial pulse is higher in frequency and arrives with a polarization suggesting a direction of travel that is 30° away from the azimuth from receiver to source. This section is focusing on a match to the longer-period displacement records which can be attained with a two-dimensional model, as discussed above, so the misfit with the initial pulse is not investigated in this paper.

A moment of 1.2×10^{26} dyne-cm is found by matching the amplitude of the synthetic in Figure 12C with the displacement record, which is similar to the result of 1.1×10^{26} found by Burdick and Mellman (1976) from teleseismic body waves and also by Butler (1983) from long-period surface waves.

Profiles for a single layer that dips down away from the source are shown in Figure 13 both to reaffirm the accuracy of our methods and to investigate the effect of dipping layers. The agreement in waveform and amplitude is excellent (see Helmberger *et al.*, 1985, for method). The initial arrival has the same frequency content as the source, but the later arrivals have higher frequency content. This phenomenon may be qualitatively understood as follows. In the geometrical ray limit, energy is trapped in the layer when it is refracted by the dipping interface past the critical angle. In the low-frequency limit, the energy is not affected by the thin layer.

The depth sensitivity of the seismograms is investigated by the GRT method (Helmberger *et al.*, 1985) in Figure 14. The GRT method is considerably faster than the FD method and generally can treat higher frequencies, so when the structure is simple enough, the GRT method is preferred.

Seismograms for the flat-layered case vary much more than they do for the dipping-layer case when the source depth changes. The depth sensitivity is an important issue. Sibson (1982) argues that one would expect the most moment release from the deeper parts of the fault plane. McGarr (1984) presents data that suggest that peak accelerations and velocities depend strongly on focal depth. For the Borrego Mountain earthquake, Heaton and Helmberger (1977) postulate a component of moment release in the shallow sediments to generate enough long-period energy to match the data. With the more realistic structure derived from the refraction profile, there is instead too much long-period energy 30 to 40 sec into the record in Figure 12c, so the need for a shallow component of moment is no longer as evident.

The structure about Borrego Mountain has considerable variations in all three dimensions, as may be seen by the structures shown on Figure 9 or by the various cross-sections in Fuis *et al.* (1983). This variation may also be seen by noting in the radial and tangential components of the El Centro record shown in Figure 10 that both the initial *SH* pulse and the later portion of the Love wave approach El Centro off-strike by up to 30°. As a result, it is not clear what is the appropriate velocity structure to use for modeling the El Centro record.

Many parameters could be perturbed in the attempt to improve the fit to the data. The time function, source finiteness, and velocity structure are not known beyond a shadow of a doubt. The seismogram in Figure 12e, generated from model C with the velocity in the top 1.8 km increased by 20 per cent, illustrates that small changes in structure can cause significant differences in the synthetic seismogram. Figure 14 shows, however, that the source finiteness does not make nearly as large a difference as in the flat-layer case. We suspect that the source time function and the structure are the primary determinants of the seismogram, and we do not know the three-dimensional structure well enough to uniquely determine the time function from the El Centro record. With just the one station used in this study, the source finiteness is difficult to investigate.

The good agreement between the data and the synthetic seismogram shows that incorporating the known two-dimensional structure can lead to improved prediction of path effects on long-period strong ground motion.

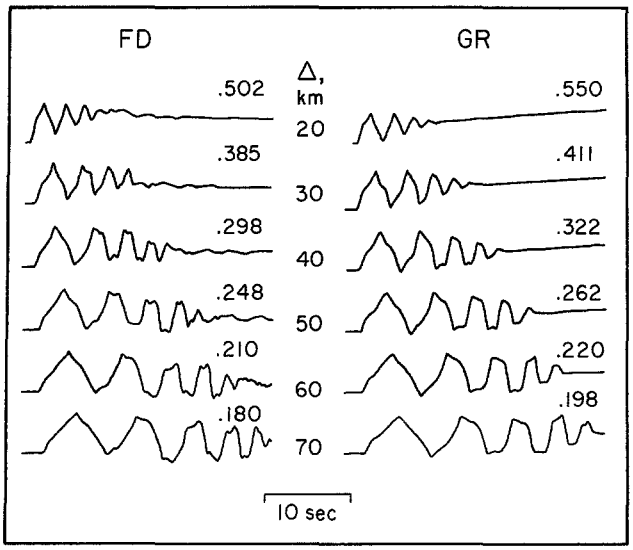

FIG. 13. Profiles for a single layer shows dips down 2.8° from the horizontal away from the source. The layer is 0.3-km-thick directly above the source. The source is 6 km below the surface. A trapezoidal time function of 0.3, 0.3, 0.3 sec has been convolved into both suites of seismograms. The seismograms on the *left* are generated by the FD method described above; those on the *right* are from a generalized ray method.

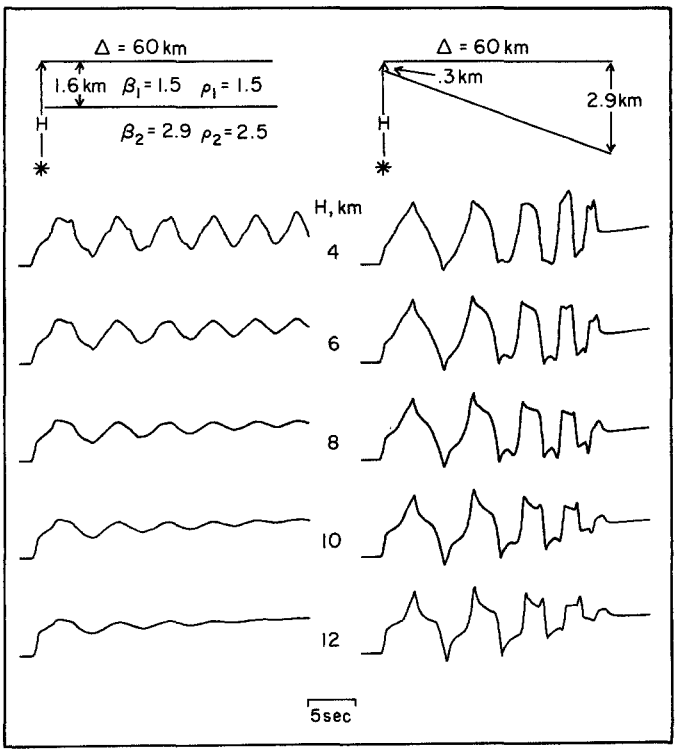

FIG. 14. Profiles for a single layer shows either flat (*left*) or dips (*right*). The geometries are given at the *top* of the figure. Note that the layer thickness is the same under the station in both cases. A trapezoidal time function of 0.2, 0.2, 0.2 sec has been convolved into both suites of seismograms.

CONCLUSIONS

The FD approach with the line to point source mapping shown to work above has many advantages. *SH* synthetic seismograms for an explosion or earthquake can be constructed at least out to 100 wavelengths from the source. The medium can have arbitrary velocity and density variations, including, of course, dipping and curved boundaries, velocity and density gradients, and low-velocity zones.

This approach has limitations. The model must be two-dimensional. In principle, three-dimensional FD elastic wave propagation codes are easy to formulate, but to be practical they require now unattainable computer memory and speed. Inversion schemes are difficult due both to the multiplicity of free parameters and the expense of many runs of a large FD program. Q is assumed to be infinite. Despite these limitations, this method can attack problems that are difficult or impossible to address by other methods.

The proposed line to point source mapping has more general applicability as well. It is reversible; i.e., point source seismograms can be converted to line source seismograms. This property may be useful for techniques that are simplest to apply to line source seismograms. Also, this method may be easily extended to model *P-SV* energy propagation (Vidale *et al.*, 1985, in preparation).

Once the path effects are known, source characteristics may be examined with more confidence. For the Borrego Mountain event, the teleseismic and long-period El Centro records may both be explained primarily by a single point dislocation near a depth of 8 km.

ACKNOWLEDGMENTS

This work was partly supported by Air Force-Cambridge Grant F19628-83-K-0010. J. E. V. was supported by an NSF Fellowship. Art Frankel aided in the development of the FD program. We thank Heidi Houston and an anonymous reviewer for their suggestions.

REFERENCES

Alford, R. M., K. R. Kelley, and D. M. Boore (1974). Accuracy of finite-difference modeling of the acoustic wave equation, *Geophysics* **39,** 834–842.

Alterman, Z. and F. C. Karal (1968). Propagation of elastic waves in layered media by finite difference methods, *Bull. Seism. Am.* **58,** 367–398.

Apsel, R. J. and J. E. Luco (1983). On the Green's functions for a layered half-space, *Bull. Seism. Soc. Am.* **73,** 909–925.

Boore, D. M. (1972). Finite difference methods for seismic wave propagation in heterogeneous materials, in *Methods of Computational Physics*, Vol. 2, B. Alder, S. Fernbach, and M. Rotenberg, Editors, Academic Press, New York, 1–37.

Brown, D. and R. W. Clayton (1977). Difference approximations for forward modeling problems, Stanford Exploration Project Report 13, 90–108.

Bulter, R. H. (1983). Surface wave analysis of the 9 April 1968 Borrego Mountain earthquake, *Bull. Seism. Soc. Am.* **73,** 879–883.

Burdick, L. J. and G. R. Mellman (1976). Inversion of the body waves from the Borrego Mountain earthquake to the source mechanism, *Bull. Seism. Soc. Am.* **66,** 1485–1499.

Clayton, R. W. and B. Engquist (1980). Absorbing boundary conditions for wave equation migration, *Geophysics* **45,** 895–904.

Ebel, J. E. and D. V. Helmberger (1982). *P*-wave complexity and fault asperities: the Borrego Mountain, California, earthquake of 1968, *Bull. Seism. Soc. Am.* **72,** 413–437.

Fuis, G. S., W. D. Mooney, J. H. Healy, G. A. McMechan, and W. J. Latter (1983). A seismic refraction survey of the Imperial Valley region, California, *J. Geophys. Res.* **89,** 1165–1189.

Heaton, T. H. and D. V. Helmberger (1977). A study of the strong ground motion of the Borrego Mountain, California, earthquake, *Bull. Seism. Soc. Am.* **67,** 315–330.

Helmberger, D. V. (1983). Theory and application of synthetic seismograms, earthquakes: observations,

theory and observations. *Proceedings of the International School of Physics*, Enrico Fermi Course LXXXV, H. Kanamori and E. Boschi, Editors, North-Holland, Amsterdam, 174–217.

Helmberger, D. V. and S. D. Malone (1975). Modeling local earthquakes as shear dislocations in a layered half space, *J. Geophys. Res.* **80,** 4881–4888.

Helmberger, D. V. and D. G. Harkrider (1978). Modeling earthquakes with generalized ray theory, in *Modern Problems in Elastic Wave Propagation*, J. Miklovitch and J. D. Achenbach, Editors, John Wiley, New York, 499–518.

Helmberger, D. V., G. R. Engen, and S. P. Grand (1985). Long period wave propagation in laterally varying structure, *Geophys. J. R. Astr. Soc.* (in press).

Langston, C. A. and D. V. Helmberger (1975). A procedure for modeling shallow dislocation sources, *Geophys. J. R. Astr. Soc.* **42,** 117–130.

McGarr, A. (1984). Scaling of ground motion parameters, state of stress, and focal depth, *J. Geophys. Res.* **89,** 6969–6979.

Scott, P. and D. H. Helmberger (1983). Applications of the Kirchoff-Helmholtz integral to problems in seismology, *Geophys. J. R. Astr. Soc.* **72,** 237–254.

Sibson, R. H. (1982). Fault zone models, heat flow, and the depth distribution of earthquakes in the continental crust of the United States, *Bull. Seism. Soc. Am.* **72,** 151–163.

Swanger, H. J. and D. M. Boore (1978). Simulation of strong-motion displacements using surface-wave modal superposition, *Bull. Seism. Soc. Am.* **68,** 907–922.

SEISMOLOGICAL LABORATORY
ROOM 252-21
CALIFORNIA INSTITUTE OF TECHNOLOGY
PASADENA, CALIFORNIA 91125
CONTRIBUTION NO. 4015

Manuscript received 25 March 1985